

## Electrostatically Driven Polarization Flop and Strain-Induced Curvature in Free-Standing Ferroelectric Superlattices

Li, Yaqi; Zatterin, Edoardo; Conroy, Michele; Pylypets, Anastasiia; Borodavka, Fedir; Björling, Alexander; Groenendijk, Dirk J.; Lesne, Edouard; Caviglia, Andrea D.; More Authors

**DOI**

[10.1002/adma.202106826](https://doi.org/10.1002/adma.202106826)

**Publication date**

2022

**Document Version**

Final published version

**Published in**

Advanced Materials

**Citation (APA)**

Li, Y., Zatterin, E., Conroy, M., Pylypets, A., Borodavka, F., Björling, A., Groenendijk, D. J., Lesne, E., Caviglia, A. D., & More Authors (2022). Electrostatically Driven Polarization Flop and Strain-Induced Curvature in Free-Standing Ferroelectric Superlattices. *Advanced Materials*, 34(15), 12. Article 2106826. <https://doi.org/10.1002/adma.202106826>

**Important note**

To cite this publication, please use the final published version (if applicable). Please check the document version above.

**Copyright**

Other than for strictly personal use, it is not permitted to download, forward or distribute the text or part of it, without the consent of the author(s) and/or copyright holder(s), unless the work is under an open content license such as Creative Commons.

**Takedown policy**

Please contact us and provide details if you believe this document breaches copyrights. We will remove access to the work immediately and investigate your claim.

# Electrostatically Driven Polarization Flop and Strain-Induced Curvature in Free-Standing Ferroelectric Superlattices

Yaqi Li,<sup>\*</sup> Edoardo Zatterin, Michele Conroy, Anastasiia Pylypets, Fedir Borodavka, Alexander Björling, Dirk J. Groenendijk, Edouard Lesne, Adam J. Clancy, Marios Hadjimichael, Demie Kepaptsoglou, Quentin M. Ramasse, Andrea D. Caviglia, Jiri Hlinka, Ursel Bangert, Steven J. Leake, and Pavlo Zubko<sup>\*</sup>

The combination of strain and electrostatic engineering in epitaxial heterostructures of ferroelectric oxides offers many possibilities for inducing new phases, complex polar topologies, and enhanced electrical properties. However, the dominant effect of substrate clamping can also limit the electromechanical response and often leaves electrostatics to play a secondary role. Releasing the mechanical constraint imposed by the substrate can not only dramatically alter the balance between elastic and electrostatic forces, enabling them to compete on par with each other, but also activates new mechanical degrees of freedom, such as the macroscopic curvature of the heterostructure. In this work, an electrostatically driven transition from a predominantly out-of-plane polarized to an in-plane polarized state is observed when a  $\text{PbTiO}_3/\text{SrTiO}_3$  superlattice with a  $\text{SrRuO}_3$  bottom electrode is released from its substrate. In turn, this polarization rotation modifies the lattice parameter mismatch between the superlattice and the thin  $\text{SrRuO}_3$  layer, causing the heterostructure to curl up into microtubes. Through a combination of synchrotron-based scanning X-ray diffraction imaging, Raman scattering, piezoresponse force microscopy, and scanning transmission electron microscopy, the crystalline structure and domain patterns of the curved superlattices are investigated, revealing a strong anisotropy in the domain structure and a complex mechanism for strain accommodation.

## 1. Introduction

In epitaxial heterostructures involving ferroelectric oxides that exhibit a strong coupling between strain and electrical polarization, the combination of mechanical and electrostatic boundary conditions offers tremendous opportunities for designing novel artificially layered materials with greatly enhanced or wholly new functionalities. Strain engineering alone can be used to achieve dramatic enhancements of the transition temperature of ferroelectrics, control the type and arrangement of ferroelastic domains, and even stabilize ferroelectricity in nominally nonferroelectric materials.<sup>[1–3]</sup> Simultaneous control of the electrostatic boundary conditions can further lead to the creation of nanoscale domain patterns with a wide range of morphologies, complex ordering, nontrivial polar topologies, and enhanced susceptibilities.<sup>[4–13]</sup>

Despite its many successes, however, conventional strain engineering, where a

Y. Li, E. Zatterin, P. Zubko  
Department of Physics and Astronomy  
University College London  
Gower Street, London WC1E 6BT, UK  
E-mail: yaqi.li.14@ucl.ac.uk; p.zubko@ucl.ac.uk

E. Zatterin, S. J. Leake  
ESRF  
The European Synchrotron  
71 Avenue des Martyrs, Grenoble 38000, France

M. Conroy  
Department of Materials  
Imperial College London  
Exhibition Road, London SW7 2AZ, UK

 The ORCID identification number(s) for the author(s) of this article can be found under <https://doi.org/10.1002/adma.202106826>.

© 2022 The Authors. Advanced Materials published by Wiley-VCH GmbH. This is an open access article under the terms of the Creative Commons Attribution License, which permits use, distribution and reproduction in any medium, provided the original work is properly cited.

M. Conroy, U. Bangert  
Department of Physics  
Bernal Institute  
University of Limerick  
Limerick V94 T9PX, Ireland

M. Conroy, P. Zubko  
London Centre for Nanotechnology  
17–19 Gordon Street, London WC1H 0HA, UK

A. Pylypets, F. Borodavka, J. Hlinka  
Institute of Physics of the Czech Academy of Sciences  
Na Slovance 2, 18221 Praha 8, Czech Republic

A. Björling  
MAX IV Laboratory  
Lund SE-221 00, Sweden

D. J. Groenendijk, E. Lesne, A. D. Caviglia  
Kavli Institute of Nanoscience  
Delft University of Technology  
P.O. Box 5046, Delft GA 2600, The Netherlands

DOI: 10.1002/adma.202106826

thin film or multilayer is strained through coherent epitaxy on a crystalline substrate, is also rather restrictive. The accessible strain states are determined by the lattice parameters of a limited number of available substrates. Once deposited, the rigid clamping to the substrate hinders any lateral lattice expansion or contraction of the film, thereby reducing its electromechanical response.<sup>[14]</sup> The substrate clamping also suppresses any elastic interactions between the individual components of a multilayer, preventing access to not only the continuous range of strain states that would otherwise be available through the elastic competition between the individual layers, but also to the much richer phase space opened up by 3D deformations of the heterostructure. Furthermore, the dominant effect of the substrate clamping means that electrostatic boundary conditions usually play only a secondary role in determining the overall polarization state, thus limiting the power of electrostatic engineering.

To lift the above restrictions and harness the full potential of strain and electrostatic engineering, the epitaxial multilayers must be released from their underlying substrates. One way to achieve this is to deposit an epitaxial sacrificial layer between the substrate and the multilayer of interest, and subsequently etch it away. While numerous sacrificial layer materials have been explored in the past, the recent demonstration that  $\text{Sr}_3\text{Al}_2\text{O}_6$  is both water-soluble and highly compatible with the perovskite structure,<sup>[15]</sup> has launched a new wave of interest in free-standing oxide films and heterostructures. Using this approach, large-area free-standing films as thin as a few perovskite monolayers have been successfully produced, giving unprecedented access to studies of the electrical and mechanical properties of oxides in the ultrathin limit.<sup>[16–23]</sup> Free-standing ferroelectric films, for example, are found to exhibit giant elastic responses, usually mediated by the formation and rearrangement of ferroelectric domains.<sup>[18]</sup> However, while important insight into the role of domains has been gained from phase field calculations<sup>[18,20,24]</sup> direct observation of these domain structures and their rearrangements remains challenging.

In this work, we investigate free-standing superlattices of  $\text{PbTiO}_3$  and  $\text{SrTiO}_3$  with a  $\text{SrRuO}_3$  bottom electrode. We find that for sufficiently thin  $\text{SrTiO}_3$  layers, releasing the superlattice

film from the substrate leads to a large contraction of its average out-of-plane lattice parameter and a concomitant reorientation of the polarization into the plane of the film. We attribute this polarization “flop” to the sudden change in the balance between the electrostatic and elastic interactions, as in the absence of substrate clamping, the ultrathin  $\text{SrTiO}_3$  layers within the superlattice are unable to provide sufficient compression to stabilize an out-of-plane polarization against the action of its own depolarizing field. In turn, the appearance of an in-plane polarization creates a large mismatch between the lattice constants of the superlattice and the bottom  $\text{SrRuO}_3$  electrode, causing the whole structure to curl up into microtubes with a well-defined radius of curvature. Using a combination of laboratory and synchrotron X-ray diffraction, piezoresponse force microscopy (PFM), Raman scattering and transmission electron microscopy, we investigate the domain structures in such curved superlattices, revealing an unusual asymmetry in the populations of in-plane domains, and the role of domains in accommodating the macroscopic curvature of the free-standing heterostructure.

## 2. Free-Standing Ferroelectric Superlattices

Superlattices consisting of 14 unit cells (uc) of  $\text{PbTiO}_3$  and  $n$  unit cells of  $\text{SrTiO}_3$  per period (denoted as  $(14|n)$  hereafter) and  $\text{SrRuO}_3$  bottom electrodes were deposited on  $(001)\text{-SrTiO}_3$  substrates buffered with sacrificial  $\text{Sr}_3\text{Al}_2\text{O}_6$  layers, as described in the Experimental Section. Here, we focus on a  $(14|3)$  superlattice with 3-uc-thick  $\text{SrTiO}_3$  layers and 12 repetitions of the superlattice period. For comparison, the results for a  $(14|6)$  superlattice with ten repetitions, where the  $\text{SrTiO}_3$  layers are twice as thick, are reported in Supporting Information.

Laboratory X-ray diffraction reciprocal space mapping of the as-grown film on the  $\text{SrTiO}_3$  substrate around the pseudocubic perovskite  $\mathbf{103}_{\text{pc}}$  peak (Figure 1a) reveals that while the superlattice has grown epitaxially, its average in-plane lattice parameter ( $\approx 3.93$  Å) is larger than that of the substrate (3.905 Å), indicating partial strain relaxation. The average out-of-plane lattice parameter for the  $(14|3)$  superlattice is  $(3.993 \pm 0.004)$  Å, which is also smaller than expected for superlattices coherently strained to  $\text{SrTiO}_3$ .<sup>[25]</sup> Despite the partial strain relaxation, the  $\text{PbTiO}_3$  layers in the superlattice remain under compressive strain relative to the cubic phase, and therefore favor a predominantly out-of-plane polarization.<sup>[26]</sup> The superlattice peaks are also accompanied by in-plane satellites characteristic of  $180^\circ$  domains that form to minimize the depolarizing field arising from the polarization discontinuity at the  $\text{PbTiO}_3/\text{SrTiO}_3$  interfaces.<sup>[4,25]</sup> The corresponding domain periodicity is approximately 10 nm with preferential ordering along  $\langle 100 \rangle_{\text{pc}}$ , suggesting a stripe-like or bubble-like domain morphology, as previously reported for superlattices on  $\text{SrTiO}_3$ .<sup>[11,27]</sup> We note that due to the slightly larger in-plane lattice parameter the exact polarization profile (e.g., magnitude of the in-plane polarization components and the “vortex aspect ratio”) is likely to be intermediate between that observed in superlattices on  $\text{SrTiO}_3$  and  $\text{DyScO}_3$  substrates.<sup>[8,11,27]</sup> Atomic force microscopy (AFM) measurements of the sample topography (Figure S1, Supporting Information), reveal a surface root-mean-square roughness of less than one unit cell, indicating that the superlattices deposited on the substrate are flat.

A. J. Clancy  
Department of Chemistry  
University College London  
20 Gordon Street, London WC1H 0AJ, UK

M. Hadjimichael  
Department of Quantum Matter Physics  
University of Geneva  
Geneva 1211, Switzerland

D. Kepaptsoglou, Q. M. Ramasse  
SuperSTEM Laboratory  
SciTech Daresbury Campus  
Daresbury WA4 4AD, UK

D. Kepaptsoglou  
Department of Physics  
University of York  
York YO10 5DD, UK

Q. M. Ramasse  
Schools of Chemical and Process Engineering  
& Physics and Astronomy  
University of Leeds  
Leeds LS2 9JT, UK

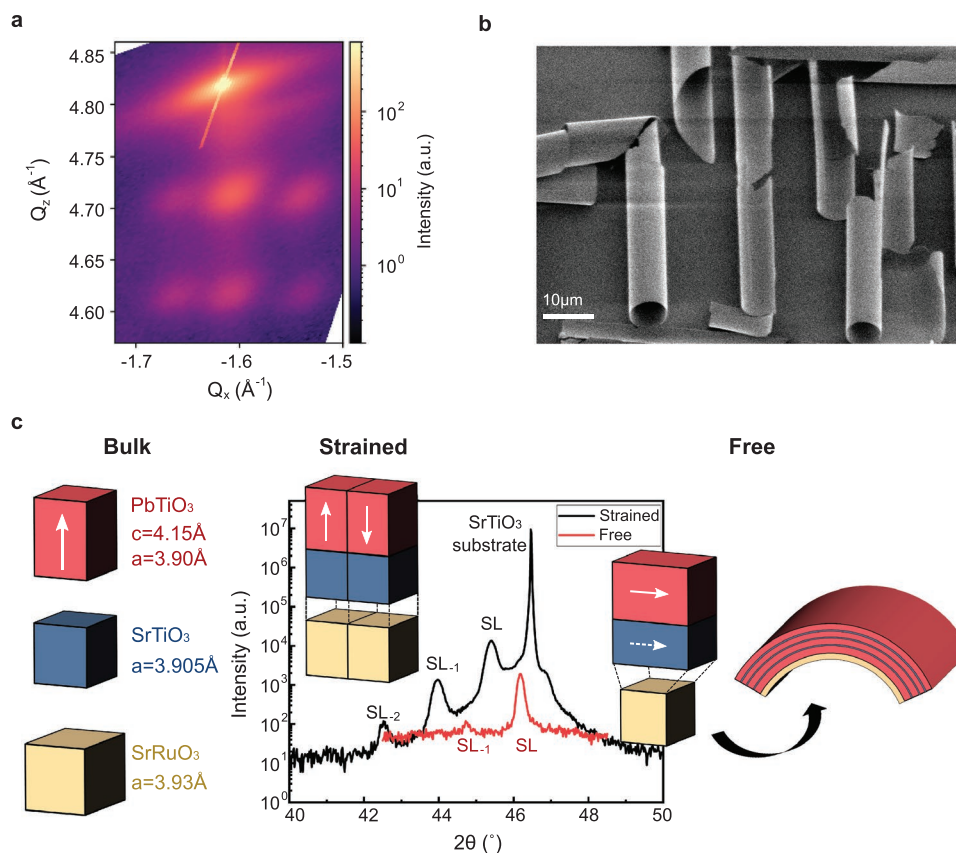


**Figure 1.** a) Reciprocal space map for the strained superlattice around the  $\bar{1}03$  reflection of the  $\text{SrTiO}_3$  substrate, showing two superlattice reflections, each accompanied by a set of in-plane satellites due to domains with period  $\approx 10$  nm. b) Scanning electron microscopy image of the free-standing superlattices curled up into tubes of radius  $\approx 4$   $\mu\text{m}$ . c) XRD  $\theta$ - $2\theta$  scans for the strained and free-standing superlattice films. Schematics show: the relationship between the lattice parameters for the bulk materials (left); favored polarization configuration for the strained heterostructure (middle inset); and the mismatch between the in-plane lattice parameters of the free-standing superlattice and the bulk lattice parameter of the  $\text{SrRuO}_3$  electrode, which causes the heterostructure to bend (right).

Each superlattice was then immersed in deionized water at room temperature to etch away the sacrificial layers, detach the heterostructure from the substrate and transfer it onto the desired support. The transfer process is summarized schematically in Figure S2, Supporting Information. A scanning electron microscopy (SEM) image of the released free-standing (14|3) superlattice on a poly(dimethylsiloxane) polymer support layer is shown in Figure 1b. The sample is found to break up into pieces of varying sizes with edges along the crystallographic  $\langle 100 \rangle$  directions. The individual fragments bend or roll up into microtubes with single or multiple windings, depending on their sizes. By contrast, flat millimeter-sized free-standing films are obtained for the (14|6) superlattice using the same method, as shown in Figure S3a, Supporting Information, indicating that the breaking up of the (14|3) superlattice is related to its tendency to curl up rather than due to damage during the transfer process.

### 3. Electrostatically Driven Polarization Flop and Strain-Induced Curvature

Figure 1c shows the  $\theta$ - $2\theta$  scans around the  $002_{\text{pc}}$  reflection for the (14|3) superlattice before and after release. Upon release, the

overall intensity of the diffraction signal is greatly reduced due to the bending of the rolled-up free-standing film fragments, which rotates most of the film volume out of the Bragg condition. The superlattice structure remains intact, as evidenced by the presence of a faint superlattice satellite labeled  $\text{SL}_{-1}$ .

The most striking effect of releasing the film from the substrate is the large shift of the diffraction peaks to higher  $2\theta$  values, indicating a large reduction in the average out-of-plane lattice parameter from  $(3.993 \pm 0.004)$   $\text{\AA}$  for the strained film to  $\approx 3.93$   $\text{\AA}$  for the released film. The reduced out-of-plane lattice parameter suggests that the longer  $c$ -axis and hence the polarization of the ferroelectric layers has flopped from out-of-plane to in-plane. This is indeed expected from electrostatic considerations, as an in-plane polarization eliminates any depolarizing field due to polarization discontinuities at the  $\text{PbTiO}_3/\text{SrTiO}_3$  interfaces (including any stray fields from multidomain states). The corresponding reduction in electrostatic energy, however, comes at the increased cost of the elastic energy required to stretch the  $\text{SrTiO}_3$  lattice in-plane to maintain structural coherence.

By contrast, the average out-of-plane lattice constant for the (14|6) superlattice remains largely unchanged when it is detached from the substrate, decreasing only slightly from

( $3.983 \pm 0.001$ ) to ( $3.974 \pm 0.001$ ) Å (Figure S3b, Supporting Information). Faint domain satellites are observed in the RSM (Figure S4b, Supporting Information), indicating that the periodic domain structure is retained in the unclamped film. This suggests that the thicker SrTiO<sub>3</sub> layers in the (14|6) sample tip the balance between the elastic and electrostatic energies in favor of a predominantly out-of-plane polarization, while in the (14|3) superlattice, the energy cost of the depolarizing field dominates over the elastic energy and forces the polarization into the plane of the film.

As a consequence of the polarization rotation, the in-plane lattice parameter elongates, and a large mismatch must develop between the in-plane lattice constants of the superlattice and the SrRuO<sub>3</sub> bottom electrode. This causes the heterostructure to bend toward the SrRuO<sub>3</sub> layer as both components try to recover their natural (bulk-like) lattice constants (Figure 1c).<sup>[28]</sup> We speculate that during the initial stage of the release process, when most of the film is still constrained by the substrate, the lattice can only elongate along the direction perpendicular to the released front, thereby setting the initial direction of the in-plane polarization and hence the direction of the bending. As the etching continues, the released portion of the film rolls up to form a tube. All tubes have a radius of approximately 4 μm.

The same radius of curvature is also observed for the smaller bent flakes that are not wide enough to form a complete tube, while wider sheets wind multiple times as a scroll. However, once the substrate constraint is fully released, the polarization in the PbTiO<sub>3</sub> is unlikely to remain entirely along the curvature direction as this would involve a very large strain in the SrTiO<sub>3</sub> layers. As we shall see, domains of orthogonal polarization form, leading to an  $a_1/a_2$  domain pattern.

#### 4. Probing Domain Asymmetry with Raman Scattering and Piezoresponse Force Microscopy

To gain further evidence of the in-plane polarization, we have performed Raman scattering measurements on a set of tubes and curved flakes. The Raman spectra of a rolled up (14|3) superlattice collected in reflection geometry at normal incidence are shown in Figure 2 as a function of the angle  $\phi$  between the light polarization and the long axis of the tube. The corresponding spectra for a (14|6) superlattice are shown in Figure S5, Supporting Information. All the observed peaks appear at positions close to those of bulk PbTiO<sub>3</sub>, which has  $3A_1+4E+B_1$  Raman active modes.<sup>[29,30]</sup> In bulk PbTiO<sub>3</sub>, the B<sub>1</sub> mode is nominally

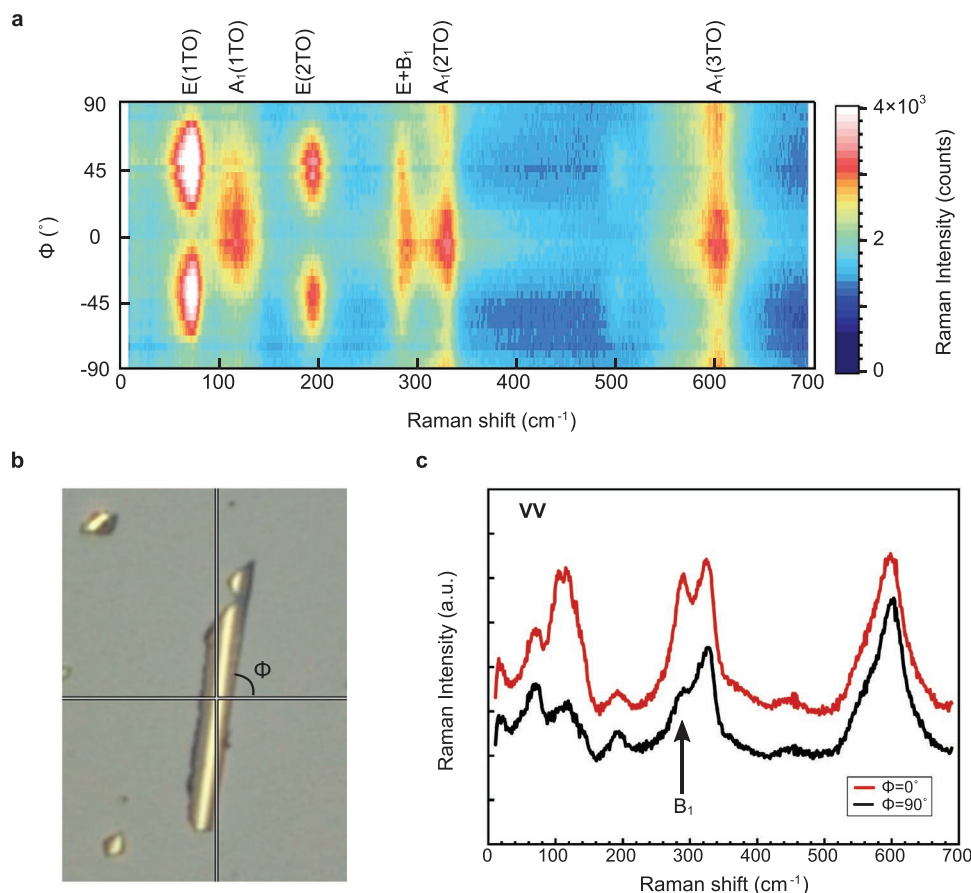


**Figure 2.** a) Raman spectra obtained in VV configuration (with parallel alignment of the incident and scattered light polarizations) as a function of the angle  $\phi$  between the light polarization and the tube axis, as defined in panel (b). c) Raman spectra for  $\phi = 0^\circ$  and  $\phi = 90^\circ$ . The B<sub>1</sub> mode is silent when the light and ferroelectric polarizations are parallel. The asymmetry in the relative intensity of the B<sub>1</sub> peak for  $\phi = 0^\circ$  and  $\phi = 90^\circ$  implies an asymmetry in the  $a_1$  and  $a_2$  domain populations.

silent when the light polarization is parallel to the  $c$  axis. For the (14|6) superlattice, the  $B_1$  mode exhibits a fourfold symmetry with intensity maxima at  $\phi = 0^\circ, 90^\circ, 180^\circ,$  and  $270^\circ$ , while the intensity of the  $A_1(\text{TO})$  mode is independent of  $\phi$ , suggesting that the polar axis of  $\text{PbTiO}_3$  points predominantly out-of-plane, in agreement with the XRD data. For the (14|3) superlattice, however, a twofold symmetry is observed instead, with the relative  $B_1$  mode intensity being significantly higher for  $\phi = 0^\circ$  than for  $\phi = 90^\circ$ . This is consistent with an in-plane polarization arrangement and further suggests that there is a large asymmetry in the relative sizes of  $a_1$  and  $a_2$  domains (i.e., domains with the polarization tangential to the curvature and along the axis of the tube respectively). Scattering by the  $B_1$

mode in the geometry with parallel polarizers is higher when the polarizers are along the long edge of the tube, indicating that the signal originates from the  $a_1$  domains with the polarization tangential to the tube curvature. Thus, the  $a_1$  domains must be significantly larger than the  $a_2$  domains and the polarization orientation initially imposed by the release process remains dominant.

In order to probe the domain structure directly, we turn to piezoresponse force microscopy. No clear vertical PFM signal is observed, except for the contrast due to the cantilever buckling effect.<sup>[31,32]</sup> This confirms that the polarization has rotated from out-of-plane to in-plane, which naturally eliminates the depolarization field. **Figure 3a** shows  $4.3 \mu\text{m} \times 4.3 \mu\text{m}$  images of lateral

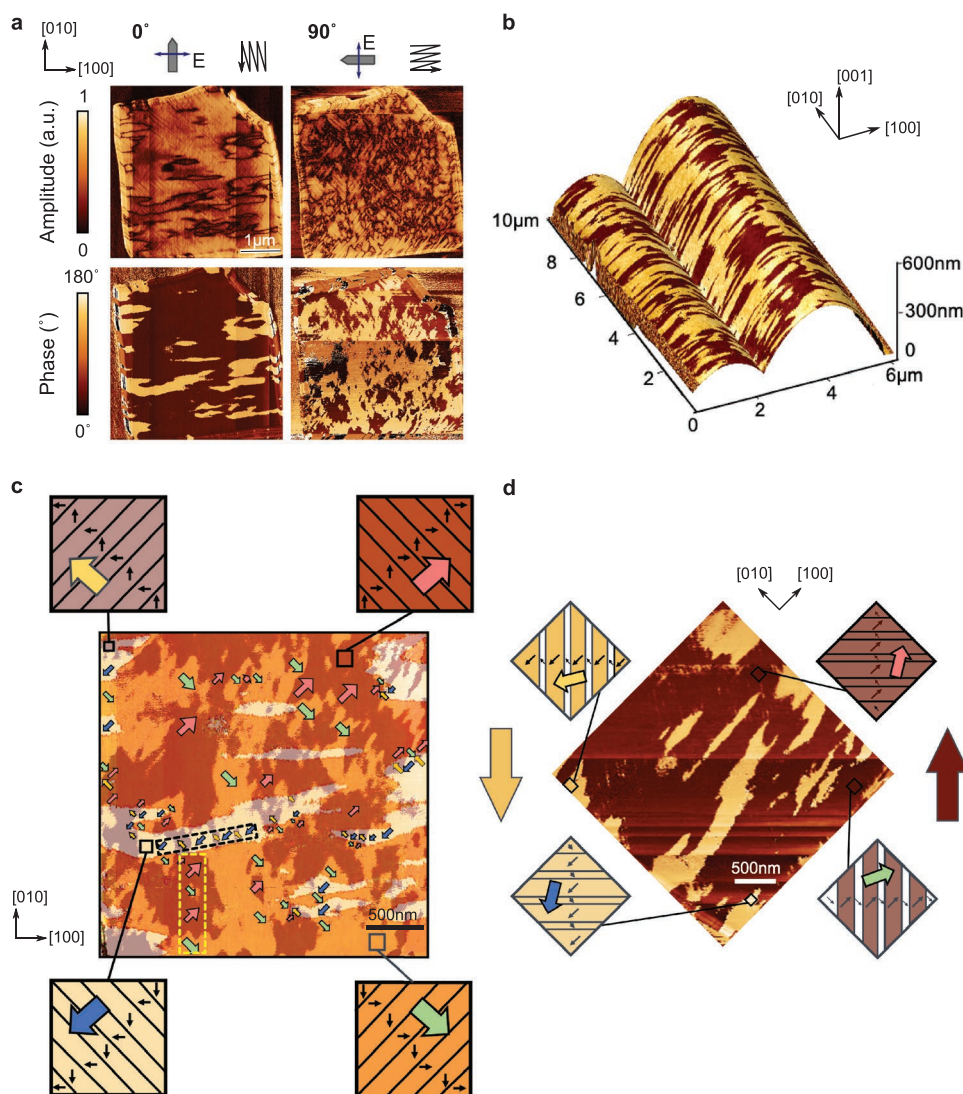


**Figure 3.** a) Lateral PFM amplitude and phase images for two different orientations of the cantilever with respect to the sample. Measurements at  $0^\circ$  and  $90^\circ$  probe polarization components parallel to  $[100]$  and  $[010]$  respectively. b) Lateral PFM phase overlaid on the surface topography for two adjacent flakes with a larger aspect ratio, demonstrating the alignment of the streaky features with the sample curvature direction. c) Superposition of PFM phase images in (a) obtained at  $0^\circ$  and  $90^\circ$  showing the distribution of the four possible superdomain variants shown schematically to the left and right of the image, where for simplicity, the sizes of the  $a_1$  and  $a_2$  domains were assumed to be the same. The dashed black box highlights a region where the net polarizations of adjacent superdomains meet head-to-tail at the superdomain boundaries, while the dashed yellow box shows a head-to-head/tail-to-tail arrangement. d) Lateral PFM phase image obtained with the cantilever at  $\approx 45^\circ$  to the  $[100]$  direction, showing the same features as the  $0^\circ$  image in (a). This is consistent with an asymmetry in the size of the  $a_1$  and  $a_2$  domains, as discussed in the main text.

PFM amplitude and phase. This sample is a square fragment from an approximately  $4\ \mu\text{m} \times 22\ \mu\text{m}$  cylindrically curved flake with the cylinder axis along one of the cubic directions that we henceforth define as [010]. In the amplitude image, there are two sets of lines: faint straight lines and dark irregular lines, corresponding to two types of domain walls in our system. The straight domain walls are crystallographically defined to be along  $\langle 110 \rangle$  as expected for in-plane  $a_1/a_2$  domains with  $90^\circ$  domain walls. The period of these  $a_1/a_2$  domains is  $\approx 33\ \text{nm}$ . The  $a_1/a_2$  domains are arranged in superdomains, each with a single orientation of the  $a_1$  and  $a_2$  domains and uniform contrast in the phase image that corresponds to the component of the net superdomain polarization perpendicular to the cantilever axis. The dark irregular lines in the amplitude images correspond to superdomain walls that separate individual superdomains.<sup>[33–35]</sup>

Since lateral PFM is only sensitive to the polarization component perpendicular to the cantilever axis, the sample was rotated by  $90^\circ$  to examine the orthogonal polarization components. An unexpected anisotropy of the superdomain pattern is observed. In the  $0^\circ$  images, where the component of polarization along [100] is probed, the superdomains appear as large, elongated stripes. Overlaying the phase image on the sample topography, as shown in Figure 3b for another flake, reveals that these stripes follow the direction of maximum curvature of the sample. By contrast, in the  $90^\circ$  images, which probe the [010] component of polarization, the superdomains appear as a patchwork of smaller, randomly shaped regions.

If the individual  $a_1$  and  $a_2$  domains within each superdomain were of equal size, measurements of the two orthogonal components would allow the full polarization pattern to be reconstructed, resulting in the arrangement sketched in Figure 3c. Moving from one superdomain to another along [100], we encounter primarily head-to-tail boundaries between the net polarizations of the different superdomains, as exemplified by the region in the dashed black box. Head-to-tail boundaries are also observed along [010]. However, along this direction, a remarkable number of head-to-head and tail-to-tail boundaries are also observed, for example, as in the dashed yellow box.

Surprisingly, when the sample is rotated by  $45^\circ$  (Figure 3d), the PFM phase image looks very similar to that at  $0^\circ$ , which is not expected for an  $a_1/a_2$  domain structure with equal sizes of  $a_1$  and  $a_2$  domains. Instead, this observation can be understood by invoking the anisotropy in domain sizes that was previously deduced from the Raman measurements. Because individual domains are not resolved in the phase images, the phase signal in the  $0^\circ$  and  $45^\circ$  images corresponds to the [100] and [110] components of the net (or average) polarization of the superdomain, respectively. At  $0^\circ$ , the signal is therefore entirely due to the  $a_1$  domains. At  $45^\circ$ , both  $a_1$  and  $a_2$  domains have polarization components along the [110] direction. However, since  $a_1$  domains are larger than  $a_2$  domains, they dominate the PFM phase signal, and the resulting image is effectively the same as at  $0^\circ$ . The net superdomain polarization is therefore tilted away from the  $\langle 110 \rangle$  directions toward [100] or  $[\bar{1}00]$ ,<sup>[36]</sup> and the charged head-to-head and tail-to-tail arrangements should correspondingly be energetically less costly along [010] than along [100]. Locally these arrangements are likely to be accommo-

dated by a needle-like structure, with the smaller  $a_2$  domains terminating into needles.<sup>[37]</sup>

The PFM and Raman measurements thus confirm that for the (14)3 superlattice the polarization lies in the plane of the rolled-up film, but that the  $a_1$  domains with polarization along [100] are larger than the  $a_2$  domains with polarization along [010]. However, due to its surface sensitivity, PFM only probes the outer-most layers of the superlattice. To probe the structure across the entire superlattice and to investigate the role played by the domain structure in accommodating the curvature, synchrotron-based scanning X-ray diffraction microscopy (SXDM)<sup>[38]</sup> was performed on individual free-standing superlattice tubes.

## 5. Scanning X-ray Diffraction Microscopy of Superlattice Microtubes

Figure 4a shows the optical microscopy image of the probed area containing a single tube. Figure 4b shows the corresponding SXDM image obtained by using a focused X-ray beam,  $\approx 80\ \text{nm} \times 80\ \text{nm}$  full width at half maximum, incident at  $\omega = 15.2^\circ$  relative to the substrate and in the plane normal to the long axis of the tube, as sketched in Figure 4c. The 2D detector is positioned near the  $002_{\text{pc}}$  reflection and the intensity in each pixel on the detector is recorded as the sample is translated with respect to the beam along the  $x$  and  $y$  directions. In the SXDM image, the tube appears as four intensity maxima labeled A–D, which can be understood by considering the diffraction geometry illustrated in Figure 4c. When the beam hits the sample at positions A and D, the out-of-plane (radial) superlattice periodicity is being probed. The detector image corresponding to position A is shown in Figure 4d and the intensity projected onto the  $Q_z$  axis in Figure 4e. Here, four superlattice peaks are visible, with the most intense peak corresponding to the  $002_{\text{pc}}$  Bragg peak due to the average out-of-plane lattice parameter (averaged over the  $\text{PbTiO}_3$  and  $\text{SrTiO}_3$  layers). On close inspection, a broad shoulder (labeled X in Figure 4e) is also visible for  $Q_z$  values just below the  $002_{\text{pc}}$  peak, indicating that the sample also contains some regions with a larger out-of-plane lattice parameter. Note that in this geometry, the exact incidence angle is not important, as the curvature of the tube ensures that, just as in powder diffraction, the specular Bragg geometry will always be satisfied at some point on the tube for any given  $\omega$ .<sup>[39]</sup> However, the incidence angle determines the apparent width of the tube in the SXDM image of Figure 4b, where the distance between intensity maxima A and D is given by  $d/\tan\omega$ . The observed distance between A and D is  $\approx 30\ \mu\text{m}$ , consistent with the tube diameter  $d \approx 8\ \mu\text{m}$ .

When the beam is instead diffracted from positions B and C on the sample, the in-plane (tangential) lattice spacing is probed. The detector image and corresponding intensity profile along  $Q_z$  obtained at position C are shown in Figure 4f,g respectively. Two replicas of a pattern consisting of four peaks are visible. The two replicas arise from the multiple windings of the superlattice. In this case, two overlapping parts of the superlattice with a small relative tilt produce two separate patterns displaced from each other.

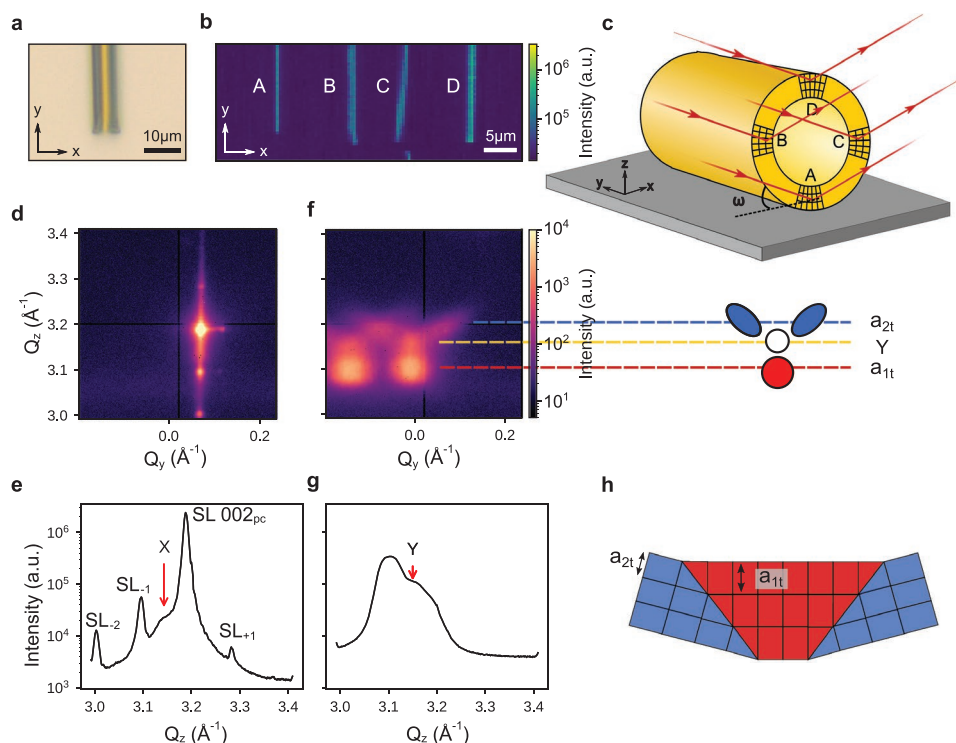


**Figure 4.** a) Optical image and b) SXDM image of a single rolled up tube. c) Schematic of the SXDM measurements for four different positions of the beam on the sample, achieved by translating the sample along  $x$  and  $y$  relative to the beam. Diffraction from positions A–D on the sample yields the corresponding intensity maxima in the SXDM image in (b). d) Intensity distribution on the detector when the beam is at positions A on the sample. The image is obtained by summing individual detector images at different positions A on the tube along the  $y$ -direction. Note that the detector plane does not correspond to a plane of constant  $Q_x$ . e) Intensity profile along  $Q_z$ , which here corresponds to the radial direction, obtained from (d) and showing several superlattice peaks and an additional feature marked X. f) Intensity distribution on the detector when the beam is at position C on the sample, obtained in the same way as the image in (d), showing two replicas of the diffraction pattern as sketched on the right. The  $a_1/a_2$  domain pattern giving rise to the peaks labeled  $a_{2t}$  and  $a_{1t}$  is also sketched. g) Intensity profile along  $Q_z$ , which in this case corresponds to the tangential direction, obtained from (f); peaks corresponding to features labelled Y and  $a_{1t}$  in (e) are visible, while the features labelled  $a_{2t}$  are too weak to be visible here. h) Schematic showing the relevant lattice constants of the  $a_1$  (red) and  $a_2$  (blue) domains probed in (f).

Within each pattern, the lower-most peak, sketched in red, corresponds to the lattice constant of the  $a_1$  domains along the polar axis, which is tangential to the tube surface. The two weaker peaks at higher  $Q_z$ , sketched in blue, correspond to the short lattice constant of the  $a_2$  domains, for which the polarization is parallel to the tube axis. The two peaks correspond to the two different twin orientations of the  $a_2$  domains and are separated by an angle of  $\approx 2.3^\circ$ . The absence of a similar splitting for the  $a_1$  domain peak is consistent with the  $a_1$  domains being the larger domains, with the lattice tilts absorbed largely by the minority  $a_2$  domains.<sup>[40]</sup>

The peak in the middle, labeled Y and visible as a shoulder in Figure 4g, is not expected for a purely  $a_1/a_2$  domain structure. We attribute this peak, and the corresponding peak X in Figure 4e to the presence of regions with out-of-plane polarization, which most likely form periodic vortex or flux closure domains akin to those observed in the original strained film and the (14)6 superlattice. The broad nature of peak X suggests that these regions are confined within a few layers of the superlattice, most likely near the bottom electrode where the compression of the lattice would favor  $c$ -domain formation.

## 6. Scanning Transmission Electron Microscopy of Domain-Structure Cross-section

To investigate the depth distribution of domains within the rolled-up superlattices, we employ scanning transmission electron microscopy (STEM) to image the cross section of a complete tube. As shown in the (secondary) SEM and STEM images of Figure 5a,b, respectively, this superlattice has rolled up into a tube with almost two complete windings. Higher-magnification annular dark-field (ADF) STEM images of a region with two windings are shown in Figure 5c,d. The atomic-number-sensitive contrast mechanism in ADF STEM imaging makes the alternating  $\text{PbTiO}_3/\text{SrTiO}_3$  layers easily recognizable as periodic dark and bright contrast bands. Upon closer inspection, it can be observed that the first one or two superlattice repetitions are not very well defined and form a rough interface with the bottom  $\text{SrRuO}_3$  layer (Figure 5d and Figure S6, Supporting Information). Core-loss electron energy loss spectroscopy (EELS) measurements indicate significant cation intermixing (Figure S7, Supporting Information) across these layers. The degradation in the quality of this interface might occur during the release process itself or be the result of the breaking of

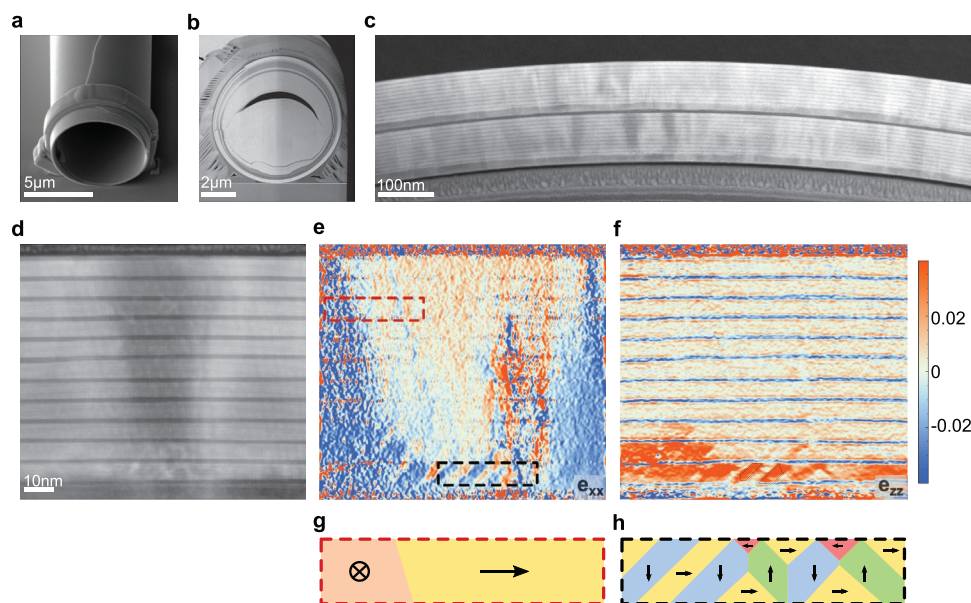


**Figure 5.** a) SEM image of a complete tube. b) ADF STEM image of sample in (a) after FIB cross-sectioning. c,d) ADF STEM images of a section of the tube in (b) with two windings, and a magnified region within one of the windings, respectively. e,f) GPA maps of the strain distribution corresponding to the image in (d) and showing regions with flux-closure-type domains with out-of-plane polarization components in the layers near the bottom electrode. g,h) Sketches illustrating the possible domain structures in regions marked by the red and black dashed boxes in (e). We note that the fine details of the flux closure regions near the interfaces or the sign of the polarization within the different domains are not resolved experimentally.

vacuum and the resulting deterioration of the  $\text{Sr}_3\text{Al}_2\text{O}_6/\text{SrRuO}_3$  bilayer between its growth using PLD and the subsequent growth of the  $\text{PbTiO}_3/\text{SrTiO}_3$  superlattice using sputtering, as described in Experimental Section of the paper. We note that while the considerable cation intermixing and interface roughness is likely to have a strong effect on the electronic properties of the  $\text{SrRuO}_3$  layer, we do not expect any qualitative changes in the mechanical behavior of the heterostructure, as the mismatch between the lattice parameters of the superlattice and the intermixed electrode layer will still result in the observed curvature. The remaining layers of the superlattice have a very well-defined superlattice periodicity and EELS measurements confirm sharp interfaces between the layers in the upper sections of the superlattice (Figure S7, Supporting Information).

In addition to the periodic dark and bright contrast due to the  $\text{SrTiO}_3$  and  $\text{PbTiO}_3$  layers respectively, there is also a weaker contrast, manifested as irregular dark and bright bands running across the thickness of the superlattice (Figure 5c). A magnified ADF image of one such region is shown in Figure 5d, while the corresponding maps of the in-plane ( $e_{xx}$ ) and out-of-plane ( $e_{zz}$ ) strain obtained from the image using geometric phase analysis (GPA)<sup>[41]</sup> are shown in Figure 5e,f.

We first focus on the top 8–9 periods of the superlattice furthest from the  $\text{SrRuO}_3$  electrode. Figure 5e shows that for these layers there is no noticeable difference between the in-plane strain in the  $\text{PbTiO}_3$  and  $\text{SrTiO}_3$  layers, consistent with a coherently strained heterostructure. However, as we move away from the top surface, there is a clear decrease in the size of the regions corresponding to larger  $e_{xx}$  and an increase in those with smaller  $e_{xx}$ . This implies a corresponding change in the size of the  $a_1$  and  $a_2$  domains respectively and therefore a tilting of the domain walls away from the crystallographically favored

{110} planes, as sketched in Figure 5g. Such tilting naturally accommodates curvature, as the width of the  $a_1$  ( $a_2$ ) domains decreases (increases) away from the top surface. However, because of the nominally {110} orientation of the domain walls, it should also cause a corresponding anticlasic curvature along the perpendicular axis, and thus cannot on its own be responsible for the observed cylindrical deformation. Thus, on closer inspection, we also find that within the regions with larger  $e_{xx}$ , the average magnitude of the in-plane strain appears to gradually decrease from top to bottom (see also Figure S8, Supporting Information), implying an additional elastic deformation of the lattice. In contrast to the  $e_{xx}$  map, a clear difference between the out-of-plane lattice parameters of the  $\text{PbTiO}_3$  and  $\text{SrTiO}_3$  layers is visible in the  $e_{zz}$  map in Figure 5f, while the presence of any gradients of  $e_{zz}$  across the superlattice thickness is not obvious.

It should be noted that two factors complicate the quantitative analysis of the in-plane strain and the identification of individual  $a_1$  and  $a_2$  domains in these STEM images. First, the {110}-orientation of the domain walls between the  $a_1$  and  $a_2$  domains means that any domain wall will appear broadened due to its projection onto the (010) imaging plane. Second, the clapping angle between the  $a_1$  and  $a_2$  domains results in relative tilts of the zone axes for the  $a_1$  and  $a_2$  domains, causing a blurring of the atomic columns for the domain which is not being imaged on zone. Additionally, one must always bear in mind the possibility of changes to the domain structure induced by the changes in dimensions following TEM sample preparation.<sup>[42,43]</sup> In particular, the small thickness of the lamella may lead to the development of depolarizing fields that destabilize the  $a_2$  domains (i.e., domains with polarization normal to the cross sections imaged in Figure 5). Nevertheless, qualitatively, the STEM data suggest that within the top 8–9 layers, the

polarization is in the plane of the layers, as already inferred from the XRD, Raman and PFM data, and that the bending of the sample is primarily accommodated by a combination of elastic strain and a depth-dependent redistribution of the sizes of the  $a_1$  and  $a_2$  domains.

For the layers near the bottom electrode, however, the compressive strain becomes sufficiently large to favor domains with out-of-plane polarization. This results in regular a/c-like domains or nanoscale flux-closure domains<sup>[7,9]</sup> that form to minimize the energy of depolarizing fields induced by any discontinuities in the out-of-plane polarization across the  $\text{PbTiO}_3/\text{SrTiO}_3$  interfaces. These domains (sketched in Figure 5h and also visible in the GPA strain maps in Figure S9, Supporting Information) have a periodicity of  $\approx 10$  nm, similar to that of the domains in the original strained superlattice (see Figure 1a). It is likely that the additional diffraction peaks X and Y observed in Figure 4 arise from these regions, as well as possible overlapping signals from the intermixed bottom  $\text{SrRuO}_3$  layer.

## 7. Domain-Structure Evolution under Mechanical Deformation

Given the multiple mechanisms involved in accommodating the curvature, one might ask: what happens if we increase the curvature of the sample? Figure 6b,c shows the strain distribution for a superlattice that was further bent by pressing on the tube with a physical SEM/FIB probe as described in Experimental Section. The radius of curvature for this section is approximately  $2\ \mu\text{m}$ , as can be seen in the overview ADF-STEM image of the structure in Figure 6d.

In the top part of the superlattice, regions of larger  $e_{xx}$  and smaller  $e_{zz}$  components, indicative of in-plane polarized  $a_1$  domains, coexist with ordered flux-closure domains that are clearly visible in the  $e_{zz}$  map. The  $a_1$  and flux-closure regions are separated by  $\{101\}$ -type superdomain boundaries, as illustrated in the sketch in Figure 6e. These superdomain boundaries are reminiscent of the tetragonal a/c twin boundaries in bulk  $\text{PbTiO}_3$  and naturally accommodate the macroscopic curvature of the superlattice through lattice tilts that can be seen in the GPA rotation map in Figure 6f.

Moving downward toward the interface with the bottom electrode, the average out-of-plane strain  $e_{zz}$  progressively increases, while the in-plane strain  $e_{xx}$  decreases, indicating a possible change in the relative fractions of the out-of-plane versus in-plane polarized domains within the flux-closure structures, as shown schematically in Figure 6e. In the bottom-most layers, flux-closure regions may coexist with  $180^\circ$  stripe or bubble domains, or even monodomain regions, although the need to minimize the depolarization field is likely to favor the former. Comparison with the data in Figure 5 and Figure S9, Supporting Information therefore suggests that increased bending of the superlattice is accommodated by movement and/or rearrangement of the boundaries between the in-plane polarized and flux-closure regions.

The coexistence of in-plane polarized regions and regions with flux-closure domains, as well as the ease of movement of the boundaries between them upon changes in curvature, suggest that for the (14|3) superlattice both states are similar in energy. This is further supported by the observation that in larger flakes, which contain regions that cannot roll up into tubes due to other mechanical constraints (e.g., see Figure S10, Supporting Information) both in-plane and out-of-plane

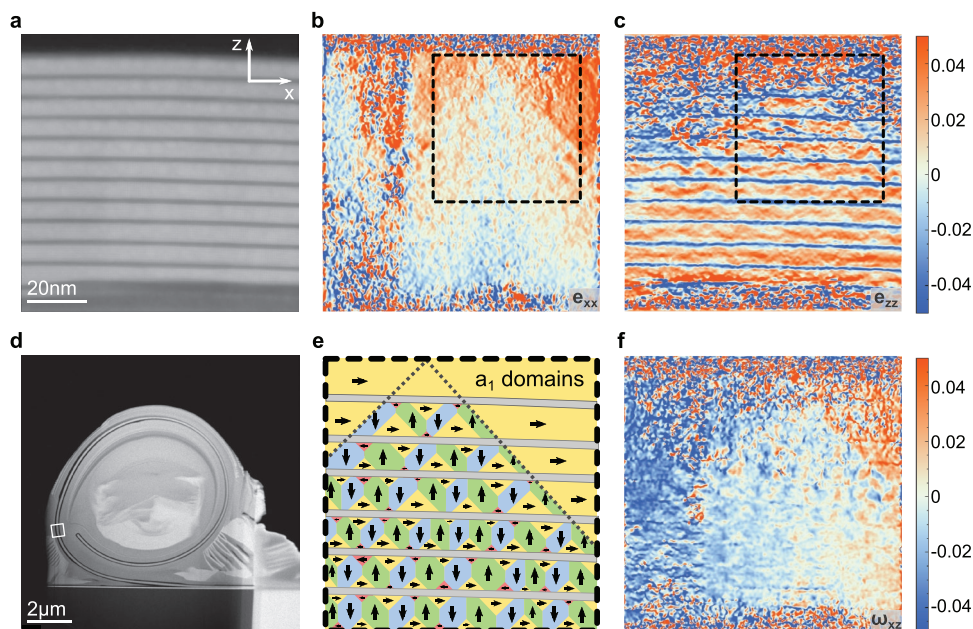


**Figure 6.** a) ADF STEM image and b,c) corresponding GPA strain maps obtained on a deformed tube in a region of higher curvature. d) Lower-magnification STEM image of the deformed tube with the white box indicating the location of the region imaged in (a). e) Schematic illustrating the possible domain arrangements within the dashed box in (b) and (c). Note, the exact local polarization patterns are not resolved experimentally. f) GPA rotation map obtained from the image in (a) illustrating the lattice tilts across the superdomains boundaries separating the  $a_1$ -domain and flux closure regions.

domains coexist, leading to a wrinkled surface morphology. Thus, in the (14)3 superlattice, electrostatics and elasticity are in close competition and the balance between them can be easily tipped in either direction not only by tailoring of the individual layer thicknesses in the superlattice, but also through a variety of external perturbations such as mechanical deformation, temperature or electric fields, paving the way for a combined strain and electrostatic engineering approach to realizing highly responsive materials.

## 8. Experimental Section

**Superlattice Growth:** The SrRuO<sub>3</sub> bottom electrode and the Sr<sub>3</sub>Al<sub>2</sub>O<sub>6</sub> sacrificial layers were grown on (001)-oriented SrTiO<sub>3</sub> substrates by pulsed-laser deposition using the deposition parameters given in ref. [44]. Typical in situ and ex situ characterization results for the SrRuO<sub>3</sub>/Sr<sub>3</sub>Al<sub>2</sub>O<sub>6</sub> bilayer are shown in Figure S11, Supporting Information. The PbTiO<sub>3</sub>/SrTiO<sub>3</sub> superlattices were then deposited using off-axis radiofrequency (rf) magnetron sputtering. PbTiO<sub>3</sub> was sputtered from a 2 inch-diameter target with 10% excess Pb (Pb<sub>1.1</sub>TiO<sub>3</sub>) to compensate for Pb volatility. A nominally stoichiometric 2-inch target was used for the deposition of SrTiO<sub>3</sub>. Both PbTiO<sub>3</sub> and SrTiO<sub>3</sub> layers were deposited with the substrate held at a temperature of 540 °C in a 180 mTorr atmosphere with an oxygen:argon ratio of 5:7, with the rf power set at 60 W.

**Laboratory and Synchrotron XRD:** The laboratory X-ray diffraction measurements were performed using a 9 kW Rigaku Smartlab high-resolution X-ray diffractometer with a 2-bounce Ge(220) monochromator and CuK $\alpha$ 1 (wavelength  $\lambda = 1.5406$  Å) radiation. The quoted domain periodicity values were obtained by fitting the domain satellites with a Gaussian. Where possible, uncertainties on the lattice parameters were determined from measurements of multiple reflections. The scanning X-ray diffraction microscopy experiment was performed at the NanoMAX beamline of the MAX IV synchrotron.<sup>[45,46]</sup> An incident X-ray energy of  $\lambda = 12.05$  keV was selected using a Si(111) double crystal monochromator with resolution  $\Delta\lambda/\lambda = 10^{-4}$ . A set of Kirkpatrick-Baez mirrors was employed to focus the incident  $\approx 10^{10}$  photons s<sup>-1</sup> into a spot of  $80 \times 80$  nm<sup>2</sup> full-width at half-maximum, as measured via a ptychography scan of a known reference object.<sup>[47]</sup> The  $2\theta$  offset was calibrated using a silicon standard sample. The sample was raster scanned relative to the focused beam in 450 nm steps using a commercial piezo scanner. A 2D Merlin Si detector<sup>[48]</sup> was placed 40 cm downstream of the sample stage and at an angular position corresponding to the 002<sub>pc</sub> superlattice reflection. At each scanned sample position, the detector was exposed for 2 ms, thus allowing a spatially-resolved map of nanodiffraction patterns to be obtained.

**AFM and PFM:** A Bruker Dimension Icon microscope was used to characterize the surface of the superlattices, and silicon AFM probes with Pt/Ir conductive coating and stiffness of 0.2 N m<sup>-1</sup> were used. For domain mapping, an AC voltage with amplitude of 1 V peak-to-peak near the contact resonance frequency was applied.

**Raman:** Raman scattering measurements were carried out using a Renishaw Raman microscope (System 1000) with 514 nm argon laser in the back-scattering geometry. The sample was mounted on a rotary microscope stage allowing for manual alignment of the sample with respect to the incident light polarization direction and subsequent automatized rotation in steps of the angle  $\phi$  using the same set up as, for example, in ref. [49].

**Electron Microscopy:** The complete superlattice microtube was initially imaged using a Thermo Fisher Scientific Helios G4 CX at 5 kV in secondary electron mode. An electron transparent cross-section of the sample was then prepared for STEM using a dual-beam focused ion beam integrated scanning electron microscope (Thermo-Fisher Scientific FEI G4 CX). Electron-beam deposited C and then Pt was first deposited at the sides of the full tubes to ensure there was no change in the curvature of the tube. It was found that if the C/Pt was deposited on the top of the tube initially the curvature of the tube changed, that is, the

tube was slightly squashed. To increase the curvature of the film further, the rolled up film was squashed by pressing with the SEM/FIB easy lift physical probe, and subsequently welded into this form by depositing C/Pt. After filling with carbon and platinum, the tubes were then cut free from the bulk sample and finally mounted onto a copper Omniprobe lift-out grid as shown in Figure 6d. The samples were thinned to electron transparency in four steps: 1) from 2  $\mu$ m to 800 nm using a 30 keV, 0.23 nA Ga ion beam; 2) 800 to 500 nm at 16 keV, 50 pA; 3) 500 to 300 nm at 8 keV, 50 pA; and 4) <100 nm at 5 keV, 46 pA, followed by a final polishing step at 2 keV and 9 pA. The STEM imaging was carried out using a Thermo-Fisher Scientific double-tilt STEM holder in the Thermo-Fisher Scientific FEI double aberration-corrected monochromated Titan Themis Z at the University of Limerick. The microscope was operated at 300 kV. The convergence angle was 24 mrad and the collection angle for ADF images was 52–200 mrad using the HAADF detector. All STEM images were processed using Thermo Fisher Scientific drift corrected frame integration Velox software to correct for drift/scan distortion.

Additional STEM imaging and EELS measurements were performed in a Nion UltraSTEM100MC monochromated dedicated STEM instrument, operated at 60 kV. The beam convergence angle used was 33 mrad with a high-angle annular dark-field detector's collection semi-angular range of 90–200 mrad. For the core-loss EELS measurements the instrument's monochromator slit was closed to obtain a zero-loss peak full-width at half-maximum of 150 meV, while the spectrometer aperture (collection) semi angle was 64 mrad. Spatially resolved electron energy loss spectroscopy measurements were performed by rastering the electron probe serially across a defined region and collecting an EEL spectrum at each point. Chemical maps were created by integrating, the spectrum intensity at each point of the acquired spectrum images over a 40 eV window above the Ti L<sub>2,3</sub> EELS edge onset after background subtraction using a power-law model. GPA analysis was conducted using the Strain++ open-source software available at <https://jjppeters.github.io/Strainpp/>. The image in Figure 1b was obtained using a JEOL JSM IT-100 scanning electron microscope operated at 3 kV with a tilt angle of 45°.

## Supporting Information

Supporting Information is available from the Wiley Online Library or from the author.

## Acknowledgements

Y.L. and P.Z. thank Sungmyung Kang for technical assistance with SEM measurements. The authors acknowledge MAX IV Laboratory for time on Beamline NanoMAX under Proposal 20190438. Research conducted at MAX IV, a Swedish national user facility, is supported by the Swedish Research council under contract 2018-07152, the Swedish Governmental Agency for Innovation Systems under contract 2018-04969, and Formas under contract 2019-02496. Electron spectroscopy work was carried out at SuperSTEM, the National Research Facility for Advanced Electron Microscopy supported by EPSRC. The authors also acknowledge use of the London Centre for Nanotechnology Atomic Force Microscope Facility. P.Z., Y.L., and E.Z. acknowledge financial support from the EPSRC (grant no. EP/S010769/1). Y.L. also acknowledges funding from the Chinese Scholarship Council. A.P., F.B., and J.H. acknowledge support from the Czech Science Foundation (project 19-28594X). M.C. acknowledges funding from the SFI Industry Fellowship (Grant No. 18/IF/6282) and Royal Society University Research Fellowship (URF-R1-201318). A.D.C. acknowledges support from the Netherlands Organization for Scientific Research (NWO/OCW) as part of the Vidi programme (Grant No. 016.Vidi.189.061). E.L. acknowledges funding from the EU Horizon 2020 research and innovation programme under the Marie Skłodowska-Curie grant agreement no. 707404. D.J.G., E.L., and A.D.C. thank Dr. Yingkai Huang for the sintering of the high-purity Sr<sub>2</sub>Al<sub>2</sub>O<sub>6</sub> target. A.J.C. thanks

the Society of Chemical Industry and The Ramsay Memorial Trust for funding.

## Conflict of Interest

The authors declare no conflict of interest.

## Data Availability Statement

High-resolution STEM images used in this study are openly available in Zenodo at <https://doi.org/10.5281/zenodo.6289588>. Other data that support the findings of this study are available from the corresponding author upon reasonable request.

## Keywords

ferroelectric domains, free-standing membranes, microtubes, strain engineering

Received: August 29, 2021

Revised: December 21, 2021

Published online: March 1, 2022

- [1] J. H. Haeni, P. Irvin, W. Chang, R. Uecker, P. Reiche, Y. L. Li, S. Choudhury, W. Tian, M. E. Hawley, B. Craigo, A. K. Tagantsev, X. Q. Pan, S. K. Streiffer, L. Q. Chen, S. W. Kirchoefer, J. Levy, D. G. Schlom, *Nature* **2004**, 430, 758.
- [2] K. J. Choi, M. Biegalski, Y. L. Li, A. Sharan, J. Schubert, R. Uecker, P. Reiche, Y. B. Chen, X. Q. Pan, V. Gopalan, L. Q. Chen, D. G. Schlom, C. B. Eom, *Science* **2004**, 306, 1005.
- [3] D. G. Schlom, L. Q. Chen, C. B. Eom, K. M. Rabe, S. K. Streiffer, J. M. Triscone, *Annu. Rev. Mater. Res.* **2007**, 37, 589.
- [4] D. D. Fong, G. B. Stephenson, S. K. Streiffer, J. A. Eastman, O. Auciello, P. H. Fuoss, C. Thompson, *Science* **2004**, 304, 1650.
- [5] P. Zubko, J. C. Wojdel, M. Hadjimichael, S. Fernandez-Pena, A. Sene, I. Luk'yanchuk, J. M. Triscone, *J. Iniguez Nat.* **2016**, 534, 524.
- [6] C. Lichtensteiger, S. Fernandez-Pena, C. Weymann, P. Zubko, J. M. Triscone, *Nano Lett.* **2014**, 14, 4205.
- [7] Y. L. Tang, Y. L. Zhu, X. L. Ma, A. Y. Borisevich, A. N. Morozovska, E. A. Eliseev, W. Y. Wang, Y. J. Wang, Y. B. Xu, Z. D. Zhang, S. J. Pennycook, *Science* **2015**, 348, 547.
- [8] A. K. Yadav, C. T. Nelson, S. L. Hsu, Z. Hong, J. D. Clarkson, C. M. Schlepuetz, A. R. Damodaran, P. Shafer, E. Arenholz, L. R. Dedon, D. Chen, A. Vishwanath, A. M. Minor, L. Q. Chen, J. F. Scott, L. W. Martin, R. Ramesh, *Nature* **2016**, 530, 198.
- [9] Y. Liu, Y. J. Wang, Y. L. Zhu, C. H. Lei, Y. L. Tang, S. Li, S. R. Zhang, J. Y. Li, X. L. Ma, *Nano Lett.* **2017**, 17, 7258.
- [10] Q. Zhang, L. Xie, G. Q. Liu, S. Prokhorenko, Y. Nahas, X. Q. Pan, L. Bellaiche, A. Gruverman, N. Valanoor, *Adv. Mater.* **2017**, 29, 1702375.
- [11] S. Das, Y. L. Tang, Z. Hong, M. A. P. Goncalves, M. R. McCarter, C. Klewe, K. X. Nguyen, F. Gomez-Ortiz, P. Shafer, E. Arenholz, V. A. Stoica, S. L. Hsu, B. Wang, C. Ophus, J. F. Liu, C. T. Nelson, S. Saremi, B. Prasad, A. B. Mei, D. G. Schlom, J. Iniguez, P. Garcia-Fernandez, D. A. Muller, L. Q. Chen, J. Junquera, L. W. Martin, R. Ramesh, *Nature* **2019**, 568, 368.
- [12] Y. J. Wang, Y. P. Feng, Y. L. Zhu, Y. L. Tang, L. X. Yang, M. J. Zou, W. R. Geng, M. J. Han, X. W. Guo, B. Wu, X. L. Ma, *Nat. Mater.* **2020**, 19, 881.
- [13] M. Hadjimichael, Y. Q. Li, E. Zatterin, G. A. Chahine, M. Conroy, K. Moore, E. N. O'Connell, P. Ondrejovic, P. Marton, J. Hlinka, U. Bangert, S. Leake, P. Zubko, *Nat. Mater.* **2021**, 20, 495.
- [14] V. Nagarajan, A. Roytburd, A. Stanishevsky, S. Prasertchoung, T. Zhao, L. Chen, J. Melngailis, O. Auciello, R. Ramesh, *Nat. Mater.* **2003**, 2, 43.
- [15] D. Lu, D. J. Baek, S. S. Hong, L. F. Kourkoutis, Y. Hikita, H. Y. Hwang, *Nat. Mater.* **2016**, 15, 1255.
- [16] R. Xu, J. Huang, E. S. Barnard, S. S. Hong, P. Singh, E. K. Wong, T. Jansen, V. Harbola, J. Xiao, B. Y. Wang, S. Crossley, D. Lu, S. Liu, H. Y. Hwang, *Nat. Commun.* **2020**, 11, 3141.
- [17] S. S. Hong, M. Gu, M. Verma, V. Harbola, B. Y. Wang, D. Lu, A. Vailionis, Y. Hikita, R. Pentcheva, J. M. Rondinelli, H. Y. Hwang, *Science* **2020**, 368, 71.
- [18] G. Dong, S. Li, M. Yao, Z. Zhou, Y.-Q. Zhang, X. Han, Z. Luo, J. Yao, B. Peng, Z. Hu, H. Huang, T. Jia, J. Li, W. Ren, Z.-G. Ye, X. Ding, J. Sun, C.-W. Nan, L.-Q. Chen, J. Li, M. Liu, *Science* **2019**, 366, 475.
- [19] L. Han, Y. H. Fang, Y. Q. Zhao, Y. P. Zang, Z. B. Gu, Y. F. Nie, X. Q. Pan, *Adv. Mater. Interfaces* **2020**, 7, 1901604.
- [20] B. Peng, R.-C. Peng, Y.-Q. Zhang, G. Dong, Z. Zhou, Y. Zhou, T. Li, Z. Liu, Z. Luo, S. Wang, Y. Xia, R. Qiu, X. Cheng, F. Xue, Z. Hu, W. Ren, Z.-G. Ye, L.-Q. Chen, Z. Shan, T. Min, M. Liu, *Sci. Adv.* **2020**, 6, eaba5847.
- [21] D. X. Ji, S. H. Cai, T. R. Paudel, H. Y. Sun, C. C. Zhang, L. Han, Y. F. Wei, Y. P. Zang, M. Gu, Y. Zhang, W. P. Gao, H. X. Huyan, W. Guo, D. Wu, Z. B. Gu, E. Y. Tsymlal, P. Wang, Y. F. Nie, X. Q. Pan, *Nature* **2019**, 570, 87.
- [22] D. Lu, S. Crossley, R. J. Xu, Y. Hikita, H. Y. Hwang, *Nano Lett.* **2019**, 19, 3999.
- [23] Z. D. Luo, J. J. P. Peters, A. M. Sanchez, M. Alexe, *ACS Appl. Mater. Int.* **2019**, 11, 23313.
- [24] C. Q. Guo, G. H. Dong, Z. Y. Zhou, M. Liu, H. B. Huang, J. W. Hong, X. Y. Wang, *Appl. Phys. Lett.* **2020**, 116, 152903.
- [25] P. Zubko, N. Jecklin, A. Torres-Pardo, P. Aguado-Puente, A. Gloter, C. Lichtensteiger, J. Junquera, O. Stephan, J. M. Triscone, *Nano Lett.* **2012**, 12, 2846.
- [26] V. G. Koukhar, N. A. Pertsev, R. Waser, *Phys. Rev. B* **2001**, 64, 214103.
- [27] M. Hadjimichael, E. Zatterin, S. Fernandez-Pena, S. J. Leake, P. Zubko, *Phys. Rev. Lett.* **2018**, 120, 037602.
- [28] O. G. Schmidt, K. Eberl, *Nature* **2001**, 410, 168.
- [29] M. D. Fontana, H. Idrissi, G. E. Kugel, K. Wojcik, *J. Phys.: Condens. Matter* **1991**, 3, 8695.
- [30] A. Bartaszyte, S. Margueron, J. Kreisel, P. Bourson, O. Chaix-Pluchery, L. Rapenne-Homand, J. Santiso, C. Jimenez, A. Abrutis, F. Weiss, M. D. Fontana, *Phys. Rev. B* **2009**, 79, 104104.
- [31] S. V. Kalinin, B. J. Rodriguez, S. Jesse, J. Shin, A. P. Baddorf, P. Gupta, H. Jain, D. B. Williams, A. Gruverman, *Microsc. Microanal.* **2006**, 12, 206.
- [32] R. Nath, S. Hong, J. A. Klug, A. Imre, M. J. Bedzyk, R. S. Katiyar, O. Auciello, *Appl. Phys. Lett.* **2010**, 96, 163101.
- [33] Y. Ivry, D. P. Chu, C. Durkan, *Nanotechnology* **2010**, 21, 065702.
- [34] L. J. McGilly, J. M. Gregg, *Appl. Phys. Lett.* **2011**, 98, 132902.
- [35] S. Matzen, O. Nesterov, G. Rispens, J. A. Heuver, M. Biegalski, H. M. Christen, B. Noheda, *Nat. Commun.* **2014**, 5, 4415.
- [36] Y. M. Jin, Y. U. Wang, A. G. Khachatryan, J. F. Li, D. Viehland, *J. Appl. Phys.* **2003**, 94, 3629.
- [37] K. Moore, M. Conroy, E. N. O'Connell, C. Cochard, J. Mackel, A. Harvey, T. E. Hooper, A. J. Bell, J. M. Gregg, U. Bangert, *Commun. Phys.* **2020**, 3, 231.
- [38] T. U. Schulli, S. J. Leake, *Curr. Opin. Solid State Mater. Sci.* **2018**, 22, 188.
- [39] B. Krause, C. Mocuta, T. H. Metzger, C. Deneke, O. G. Schmidt, *Phys. Rev. Lett.* **2006**, 96, 165502.
- [40] C. M. Foster, W. Pompe, A. C. Daykin, J. S. Speck, *J. Appl. Phys.* **1996**, 79, 1405.
- [41] M. J. Hytch, E. Snoeck, R. Kilaas, *Ultramicroscopy* **1998**, 74, 131.
- [42] G. Catalan, A. Schilling, J. F. Scott, J. M. Gregg, *J. Phys.: Condens. Matter.* **2007**, 19, 132201.

- [43] C. B. Tan, Y. Q. Dong, Y. W. Sun, C. Liu, P. Chen, X. L. Zhong, R. X. Zhu, M. W. Liu, J. M. Zhang, J. B. Wang, K. H. Liu, X. D. Bai, D. P. Yu, X. P. Ouyang, J. Wang, P. Gao, Z. L. Luo, J. Y. Li, *Nat. Commun.* **2021**, *12*, 4620.
- [44] D. Davidovikj, D. J. Groenendijk, A. M. R. V. L. Monteiro, A. Dijkhoff, D. Afanasiev, M. Siskins, M. Lee, Y. Huang, E. van Heumen, H. S. J. van der Zant, A. D. Caviglia, P. G. Steeneken, *Commun. Phys.* **2020**, *3*, 163.
- [45] U. Johansson, D. Carbone, S. Kalbfleisch, A. Björling, M. Kahnt, S. Sala, T. Stankevic, M. Liebi, A. Rodriguez Fernandez, B. Bring, D. Paterson, K. Thänell, P. Bell, D. Erb, C. Weninger, Z. Matej, L. Roslund, K. Åhnberg, B. Norsk Jensen, H. Tarawneh, A. Mikkelsen, Vogt, *J. Synchrotron Radiat.* **2021**, *28*, 1935.
- [46] A. Björling, S. Kalbfleisch, M. Kahnt, S. Sala, K. Parfeniukas, U. Vogt, G. Carbone, U. Johansson, *Opt. Express* **2020**, *28*, 5069.
- [47] F. Pfeiffer, *Nat. Photonics* **2018**, *12*, 9.
- [48] R. Plackett, I. Horswell, E. N. Gimenez, J. Marchal, D. Omar, N. Tartoni, *J. Instrum.* **2013**, *8*, C01038.
- [49] I. Rafalovskyi, M. Guennou, I. Gregora, J. Hlinka, *Phys. Rev. B* **2016**, *93*, 064110.